Ionic liquid-based electrolytes for sodium-ion batteries: tuning properties to enhance electrochemical performance of manganese based layered oxide cathode

Luciana Gomes Chagas [a,b,†], Sangsik Jeong [a,b], Ivana Hasa [a,b]* and Stefano Passerini [a,b,]*

[a] Helmholtz Institute Ulm (HIU), Helmholtzstrasse 11, 89081 Ulm, Germany

[b] Karlsruhe Institute of Technology (KIT), P.O. Box 3640, 76021 Karlsruhe, Germany

† Present address: Johnson Matthey, Blount's Court, Sonning Common, Reading, RG4 9NH, United Kingdom

Corresponding authors: stefano.passerini@kit.edu, ivana.hasa@kit.edu

Keywords:

Sodium-ion battery, ionic liquid electrolyte, P2-layered oxide cathode, NaTFSI, NaFSI

Abstract

Ionic liquids (ILs) are considered as appealing alternative electrolytes for application in rechargeable batteries, including the next-generation sodium-ion batteries, because of their safe and eco-friendly nature, resulting from their extremely low volatility. In this work, two groups of advanced pyrrolidinium based ILs electrolytes are concerned, made by mixing sodium bis(fluorosulfonyl)imide (NaFSI) or sodium tri(fluoromethanesulfonyl)imide (NaTFSI) salts with N-Methyl-N-propylpyrrolidinium bis(fluorosulfonyl)imide ($Pyr_{13}FSI$), N-Butyl-N-methylpyrrolidinium bis(fluorosulfonyl)imide ($Pyr_{14}FSI$) and N-butyl-N-methylpyrrolidinium bis(trifluoromethanesulfonyl)imide ($Pyr_{14}TFSI$). The characterization of eight different electrolytes, including single anion electrolytes and binary anions mixtures, in terms of thermal properties, density, viscosity and conductivity as well as electrochemical stability window and cycling performance in room temperature sodium cells is reported here. Among all

the blends, those containing $Pyr_{14}FSI$ outperform the others in terms of cell performance enabling the layered P2-$Na_{0.6}Ni_{0.22}Al_{0.11}Mn_{0.66}O_2$ cathode to deliver about 140 mAh g^{-1} for more than 200 cycles.

1. Introduction

The implementation of efficient energy storage systems is a global increasing interest, affecting the use of greener and environmentally friendly renewable energy alternatives needed by the modern society.[1,2] Electrochemical energy storage systems such as rechargeable batteries and supercapacitors are key components for a future sustainable energy scenario.[3] The most successful example of rechargeable batteries is the lithium-ion battery (LIB).[4] Since its first commercialization, almost three decades ago, research and investment have led to LIBs that are ten-fold cheaper than the first commercialized version while their volumetric energy has increased by a factor of three.[5,6] Nonetheless, some constraints are foreseen for LIBs on the long-term perspective, mostly concerning with the availability of raw materials. Nowadays, sodium-ion batteries (SIBs) are under development as a valid and promising, not necessarily competing, alternative to LIBs. The enthusiasm toward SIBs is mainly driven by the low cost, abundance and homogeneous distribution of the employed raw materials with respect to LIBs.[7]

Several promising materials have been proposed for both the cathode[8–11] and the anode[12–14] side of SIBs. So far, a much more limited number of studies has focused on the electrolyte, which, however, represents a key component in the electrochemical cells since it interacts with both electrodes and might limit the overall cell voltage.[15–17] Additionally, the electrolyte plays a fundamental role in the safety of the cells. The most commonly employed electrolytes in commercial LIBs and SIB prototypes employ a mixture of organic carbonates as solvent, which are known to be flammable and volatile, while the commonly used alkali metal salts ($LiPF_6$ or

$NaPF_6$) are very sensitive towards hydrolysis and have limited thermal stability.[18] In this context, alongside with solid-sate or solvent-free, polymer electrolytes,[19,20] ionic liquid (IL)-based electrolytes may play a key role for an improved safety.[21,22]

ILs represent an extraordinarily versatile class of materials with unique properties finding application in different fields such as food and bio-product industry[23], catalytic organic transformation[24], analytical separation and metal extraction[25], and lubrication[26], among others. Besides, they are also seen as potential candidates for electrolytes for secondary batteries.[21,22] The research on ILs finds its primary motivation within the green chemistry philosophy. Indeed, the substitution of the commonly employed solvents, generally including volatile organic compounds (VOCs), by non-volatile (thus greener) solvents such as ionic liquids, is a well perceived process leading to reduced waste, toxicity and hazards at the industrial scale.[27]

Some families of ILs have been investigated as electrolyte component due to their good ionic conductivity (0.1 to 5 mS cm^{-1} at 20 °C for ILs based on the pyrrolidinium cation),[28] wide electrochemical stability, and very low vapour pressure (*i.e.*, negligible volatility).[29,30] Although ILs have usually higher viscosity than the commercially used organic carbonates, leading to lower conductivities, some groups report promising results in terms of enhanced delivered capacity and cycle life of LIBs and SIBs employing IL-based electrolytes.[17,31,32] ILs are salts usually composed of at least one large, asymmetric ion. The anion is generally weakly coordinated to the cation, which is a bulky and asymmetric organic molecule, leading to a poor tendency of crystallization at room temperature.[22,33,34] ILs based on pyrrolidinium cations, such as N-methyl-N-propyl pyrrolidinium $[Pyr_{13}]^+$ and N-butyl-N-methyl pyrrolidinium $[Pyr_{14}]^+$, are appealing for battery application due to a good ionic conductivity, especially in combination with

imide-based anions, such as the bis(fluorosulfonyl)imide $[FSI]^-$ and the larger bis(trifluoromethanesulfonyl)imide anions $[TFSI]^-$.[17,35–37]

In light of the aforementioned, it is clear that each ionic liquid has some *pros* and *cons* due to the intrinsic properties of the anion and cation, and the combination between them. Therefore, in order to tune the IL properties for battery application one approach is to mix different anions, as it might favour the ionic dissociation and the viscosity, thus enhancing the Na^+ cation conductivity.[38,39] In this work, single anion electrolytes (as NaFSI in $Pyr_{14}FSI$ or NaTFSI in $Pyr_{14}TFSI$) and binary anions mixtures (for instance, NaFSI in $Pyr_{14}TFSI$) are characterized in terms of thermal properties, density, viscosity and conductivity as well as electrochemical stability window. Finally, to check their feasibility for room temperature battery applications, the electrochemical performance of the investigated electrolytes was tested in Na/P2-$Na_{0.6}Ni_{0.22}Al_{0.11}Mn_{0.66}O_2$ (NAM) cells.[40]

2. Experimental Section

2.1 Preparation of Electrolytes

The electrolytes were prepared by using commercially available sodium salts, *i.e.*, NaFSI (sodium bis(fluorosulfonyl)imide, 99.7%, Solvionic) and NaTFSI (sodium bis(trifluoromethanesulfonyl)imide, 99.5%, Solvionic), and in-house synthesized ionic liquids (ILs), namely, $Pyr_{13}FSI$ (N-Methyl-N-propylpyrrolidinium bis(fluorosulfonyl)imide), $Pyr_{14}FSI$ (N-Butyl-N-methylpyrrolidinium bis(fluorosulfonyl)imide) and $Pyr_{14}TFSI$ (N-Butyl-N-methylpyrrolidinium bis(trifluoromethanesulfonyl)imide), according to a previously developed synthesis.[35,41] Salts and ILs were extensively dried at 90 °C ($[FSI]^-$-based ILs) and 120 °C ($[TFSI]^-$-based ILs) under vacuum (by turbo-molecular pump). The prepared electrolytes, which

compositions are detailed in Table 1**,** were mixed at room temperature via magnetic stirring and dried at 50 °C under vacuum (by turbo-molecular pump). The carbonate-based electrolyte was prepared by dissolving $NaPF_6$ (sodium hexafluorophosphate, battery grade, FluoroChem) in PC (propylene carbonate, battery grade, UBE, Japan) achieving a 1 M solution.

The dried electrolytes were handled in dry room (dew point < -70 °C) or dry box (MBraun, O_2 and H_2O < 0.5 ppm).

2.2. Physical-chemical characterization of electrolytes

The ionic conductivity was determined by the automated Multiplexed Conductivity Meter equipped with a frequency analyser and a thermostatic chamber (MCS-10, BioLogic). The conductivity cells constants were determined using the 0.01 M KCl standard solution. The investigated electrolytes were loaded into sealed glass conductivity cells equipped with two platinized platinum electrodes, inside the dry box. The electrolytes conductivity was investigated within the -20 to +60 °C temperature range, with ramping steps of 5 °C per hour. The samples were kept in equilibrium at each step for at least one hour prior to measure the conductivity.

Viscosity measurements were performed in the dry room, using an Anton-Paar Physica MCR301 rheometer in the cone-plate geometry within the -20 °C to 60 °C temperature range each 10 °C applying increasing shear rates (from 100 to 2500 s^{-1}).

Differential scanning calorimetry (DSC) measurements were performed using a TA Discovery DSC series with liquid N_2 cooling. The samples were hermetically sealed in aluminium pans inside the glove box. At first, the samples were heated up from room temperature to 80 °C, and then cooled down to -150 °C. To allow full crystallization of the samples and a more reproducible thermal behavior, sub-ambient annealing was performed by

thermal cycling the samples from -150 °C to their cold crystallization temperature. A schematic illustration of the thermal cycling is depicted in Figure S1 in the Supporting Information section. Finally, samples were heated from -150 °C to 80 °C.

The thermogravimetric analysis (TGA) was performed on a Netzsch TG 209 F1 Libra device under N_2 flux from 30 to 600 °C at 10 °C min^{-1} scan rate. Samples were prepared and sealed in aluminium pans inside a glove box.

2.3. Electrode preparation

Carbon-based electrodes were made from slurries containing 80 wt.% carbon black Super C65 (TIMCAL) and 20 wt.% polivinylidene di-fluoride (PVDF 6020 Solef®, Arkema Group) dissolved in NMP (N-methyl-2-pyrrolidinone, Aldrich). The slurries were stirred for at least 4 hours, then casted on aluminium foil (20 μm, Evonik, Germany) and dried at 60 °C overnight in the oven (Binder). Disc electrodes with 12 mm diameter were cut and dried at 120 °C under vacuum for 24 h.

The synthesis of the $Na_{0.6}Ni_{0.22}Al_{0.11}Mn_{0.66}O_2$ (NAM) cathode material is reported in literature.[40] NAM electrodes were prepared by mixing the active material (NAM), Super C65 and PVDF (85:10:5 weight ratio) in NMP. The slurries were stirred for at least 4 hours, casted on aluminium foil and dried at 60 °C overnight. Disc electrodes with 12 mm diameter were cut, pressed (2.5 tons cm^{-2} for 3 seconds), and finally dried at 120 °C under vacuum for 24 h.

2.4. Electrochemical characterization

Cyclic voltammetry (CV) and linear sweep voltammetry (LSV) were employed to determine the cathodic and anodic electrochemical stability of the electrolytes using Super C65-

based electrodes assembled into Swagelok® three-electrode cells in an argon-filled glove box employing glass fiber as a separator (GF/D, Whatman) and sodium metal (99.8%, Acros Organics) as counter and reference electrodes. The measurements were performed at 20 ± 2 °C using a potentiostat (VMP Biologic Science Instruments). During the CV tests used for the determination of the cathodic stability, the cells were cycled between 3.0 V and 0.01 V *vs.* Na/Na^+, while in the LSV measurements, used to determine the anodic stability, the carbon electrode potential was increased from open circuit voltage (OCV) to 6.0 V *vs.* Na/Na^+. Both sets of measurements were performed at the scan rate of 0.1 mV s^{-1}.

A battery tester (Maccor Series 4000) was used to perform the galvanostatic cycling tests of Na/NAM cells employing the various ionic liquid electrolytes. Two-electrode coin cells were assembled in an argon filled glove box by using glass fiber separator (GF/A, Whatman) wetted by ionic liquid-based electrolyte and sodium metal as counter electrode. The tests were carried out at 20 ± 2 °C, within different voltage ranges, *i.e.* 4.6 V - 1.5 V, 4.3 V - 1.5 V and 4.0 V - 1.5 V, at a constant current of 30 mA g^{-1} (the nominal capacity is 160 mA h g^{-1}, corresponding to 0.6 equivalent of Na per mole of material).

3. Results and Discussion

A summary of the IL-based electrolytes investigated in this work is given in Table 1, including information on composition and nomenclature used within this manuscript.

Table 1

3.1 Thermal characterization of the IL-based electrolytes

Figure 1

Figure 1 shows the results of the thermal characterization of the IL-based electrolytes by TG and DSC analysis. The TG curves of the electrolytes containing NaFSI and NaTFSI salts, Figure 1 (a) and (b), show that, among all samples, the $[TFSI]^-$-based electrolyte (T-14T) presents the highest thermal stability as the weight loss for this material occurs only above 400 °C. For the F-14T electrolyte, a moderate weight loss occurs at about 300 °C, indicating the initial decomposition of the $[FSI]^-$ anion (not observed for the T-14T electrolyte). Following, an intense weight loss is detected between 400 °C and 490 °C, leading to a reduction of 90% of the initial mass of both the T-14T and T-14F samples. On the other side, the $[FSI]^-$-rich electrolytes (*i.e.*, F-13F and F-14F) exhibit thermal stability up to about 300 °C, when an intense weight loss is observed. The electrolytes with equal anions' ratios (*i.e.*, F-14FT and T-14TF) show an intermediate behaviour with the decomposition process starting at about 300 °C, typical of $[FSI]^-$ containing electrolytes, followed by an attenuated weight loss between 325 °C and 390 °C. Finally, they show a fast weight loss up to 480 °C. Based on the TGA results, the thermal stability of the investigated electrolytes is seen to clearly depend on the anion, following the order [TFSI] > [TFSI+FSI] > [FSI]. The length of the cation alkyl chain does not considerable impact the thermal decomposition, as shown by the rather comparable TG curves of the F-13F and F-14F electrolytes (Figure 1 (a)) and the T-13F and T-14F electrolytes (Figure 1 (b)). The anion, however, plays a crucial role since the sulphur-fluorine bond in $[FSI]^-$ is less stable than the carbon-sulphur bonds in $[TFSI]^-$ anions, thus reducing the thermal stability.[35] Nevertheless, all the electrolytes present a thermal stability well beyond the standard operating condition of sodium-ion batteries.

Figure 1 (c-d) shows the DSC heating traces of the investigated electrolytes. The two samples containing 90 mol% of $Pyr_{13}FSI$ (F-13F and T-13F) exhibit multiple and intense endothermic peaks suggesting their high tendency to crystallize. The most intense peaks, located at about -15 °C and -21 °C, respectively for F-13F and T-13F, correspond to the melting points (T_m) of these electrolytes. Thus, the melting point of pure $Pyr_{13}FSI$, located at -9 °C,[38] decreases upon the sodium salt addition to -15 °C and even further, -21 °C, when the second anion $[TFSI]^-$ is present. This is due to the different crystal frame strength generated by the anions' interactions.[38] In addition, in the pure $Pyr_{13}FSI$ ionic liquid, two other peaks related to solid-solid phase transitions are observed at -19 °C and -83 °C.[38] Regarding the mixtures seen in Figure 1 (c-d), the F-13F electrolyte (panel I) shows the peak at -19 °C, whereas the T-13F (panel I') shows the peak at -83 °C. Both samples, however, present a feature at -37 °C, most likely related to a new solid-solid transition. Interestingly, for both electrolytes, there is an indication of glass transition at about -50 °C suggesting the existence of amorphicity even after the sub-ambient annealing.

Pure $Pyr_{14}FSI$ shows a similar thermal behaviour to $Pyr_{13}FSI$, with a melting point peak at -18 °C, and two further peaks related to solid-solid transition at -30 °C and -45 °C.[38] By adding NaFSI salt a minor decrease of melting temperature to -27 °C is observed (panel II, Figure 1 (c)), while the solid-solid transition temperatures are not affected. By contrast, the addition of 10 mol% of NaTFSI, *i.e.*, the T-14F electrolyte, (panel II', Figure 1 (d)) inhibits the crystallization of the electrolyte. Indeed, the sample only shows a glass transition at about -96 °C. The same is true for the F-14T sample (panel III, Figure 1 (c)) that shows only a glass transition at around -81 °C. It can be concluded that the introduction of salts in the system as well as the inclusion of different ions hinders to a large extent the crystallization.

The sample containing only $[TFSI]^-$, *i.e.* T-14T (panel III' Figure 1 (d)), also exhibits the glass transition suggesting the presence of a not fully crystallized fraction, however, the crystallization of the mixture is indicated by the melting peak at -11 °C. The little exothermic feature observed at -23 °C is associated to the cold recrystallization of the amorphous fraction. Finally, the samples with mixed ionic liquids, *i.e.* F-14FT and T-14TF reported in Figure 1 (c, panel IV) and (d, panel IV'), respectively, only show a glass transition at -89 °C. To summarize, the electrolytes containing only one anion, such as for the F-13F, F-14F and T-14T, all exhibit crystallization peaks independent on the ionic liquid cation, while those having mixed anions but the same cation, such as F-14T and T-14F, do not show any evidence of crystallization, even after sub-ambient annealing. This can be explained considering the ionic asymmetry and dimensional mismatch between the $[FSI]^-$ and $[TFSI]^-$ anions.[38]

3.2. ESW of the IL-based electrolytes

Figure 2

The anodic stability of electrolytes is generally evaluated by employing inert electrodes, such as platinum or nickel,[42,43] which, however, largely overestimate the anodic stability of the electrolytes. Herein, we evaluate the ESW using carbon black-based electrodes (see Experimental Section), which simulate more realistic conditions for the electrolyte in contact with a composite cathode, which is composed of the active material (80%), conductive carbon black (Super C65, 10%) and binder (PVDF, 10%).[44] The electrolyte anodic stability is, by our own convention, determined considering the oxidative current limit of 10 $\mu A\ cm^{-2}$ as the threshold. Figure 2 reports the cathodic and anodic stability of the NaFSI (Figure 2 (a-d)) and

NaTFSI-based electrolytes (Figure 2 (e-h)). The anodic stabilities of [FSI$^-$] based electrolytes are slightly inferior than those of the [TFSI]$^-$ based ones. Indeed, as shown in Figure 2 (a-b), the F-13F and F-14F electrolytes (100% [FSI]$^-$ anion), exhibit anodic stabilities of 4.89 V and 4.72 V, which are slightly inferior to those obtained by adding 10 mol% [TFSI]$^-$, 4.92 V and 4.88 V for T-13F and T-14F electrolytes, respectively (see Figure 2 (e-f)). The lower anodic stability of the FSI-based blends is attributed to the lower stability of the sulphur-fluorine bond in [FSI]$^-$ when compared to the carbon-sulphur bond in the [TFSI]$^-$ anions.[35]

All samples with substantial fractions of [TFSI]$^-$, *i.e.*, 50 mol% or higher, show comparable values of potential onsets around 4.9 V, and about 5.0 V for the T-14T electrolyte (100% [TFSI]$^-$ anion). Nonetheless, all the investigated electrolytes exhibit an extended anodic stability of at least 4.7 V *vs.* Na^+/Na, as pointed out in Figure 2. It is worth mentioning, that according to previous studies, the formation of a stable passivation layer occurs on the aluminium current collector, leading to a limited (if any) aluminium dissolution.[45–47]

Depending on the electrolyte, the voltammetric cathodic scans (Figure 2**)** show several features occurring below 1.0 V. At very low potential (i.e., below 0.3 V) the sodium ions storage into the amorphous carbon (Super C65) structure occurs.[48] At higher voltages (0. 3 V - 1.0 V) two concomitant processes occur. The first one, highlighted by the peak at about 0.6 V, is associated to the solid electrolyte interphase (SEI) formation,[17,48] while the second process is ascribable to the surface reactivity of carbon active sites as well as the occurrence of sodium storage.[49] The cathodic onset current occurs at slightly higher potential values for the [FSI]$^-$-rich electrolytes than for the [TFSI]$^-$-rich ones, which is most likely attributable to the [FSI]$^-$ anion decomposition better contributing to the SEI film-forming properties compared to the [TFSI]$^-$ anion.[50]

3.3. Physical-chemical properties of the IL-based electrolytes

Figure 3

The transport properties and rheological behavior of the NaFSI- and NaTFSI-based electrolytes were investigated in terms of temperature dependence of conductivity and viscosity reported in the Arrhenius plots of Figure 3 (a, b) and Figure 3 (c, d), respectively. It is worth noting that, the conductivity plots do not show any indication of crystallization at the lowest temperature investigated (-20 °C), although some of them showed thermal features in the DSC analysis. This can be explained considering that during the DCS measurements a rather low temperature annealing was performed favouring crystallization.

The F-13F blend presents the highest conductivity over the whole investigated temperature range (Figure 3 (a)), being 2 mS cm^{-1} at 0 °C, 5 mS cm^{-1} at 20 °C, and up to 15 mS cm^{-1} at 60 °C. Progressively decreasing conductivities are observed for the F-14F, F-14FT and F-14T samples, offering RT conductivity values of about 3 mS cm^{-1}, 2 mS cm^{-1} and 1 mS cm^{-1}, respectively. The same trend is observed for the NaTFSI based electrolytes (see Figure 3 (b)), which conductivity decreased from 4 mS cm^{-1} to 3 mS cm^{-1}, 2 mS cm^{-1} and 1 mS cm^{-1}, respectively for the T-13F, T-14F, T-14TF and T-14T electrolytes. On average, from RT to 60 °C a 4-fold increase of conductivity is observed, while going down to 0 °C leads to a decrease of the conductivity of a factor of 3.

Figure 3 (c, d) reports the temperature dependence of viscosity. In agreement with the conductivity measurements, the viscosity trend follows the same order of ILs. At room

temperature the less viscous blend is the F-13F with a value of about 70 mPa s, followed by the F-14F, F-14FT and the F-14T with values of 90, 120, 170 mPa s, respectively.

The ionic conductivity (Figure 3 (a, b)) increase matches well the fluidity (inverse of viscosity, Figure 3 (c, d)), indicating that the ion movement is mostly affected by the viscous drag.[44] The conductivity and viscosity trends, however, deviate from the linear behaviour following the convex curvature typically described by the Vogel-Tammann-Fulcher (VTF) equation. The activation energy can be derived introducing a correction factor (T_0 (K)), as reported in Equation 1 and 2:

$$\sigma(T) = \sigma_\infty \, exp\left(-\frac{E_{a\sigma}}{K_B(T-T_0)}\right) \quad (1)$$

$$\eta(T) = \eta_\infty \, exp\left(-\frac{E_{a\eta}}{K_B(T-T_0)}\right) \quad (2)$$

T_0 is correlated to the glass transition temperature (generally 10 – 20 °C lower than the T_g measured by DSC) and is referred as zero configurational entropy. The other quantities in the equations are the ionic conductivity and viscosity at infinite temperature, *i.e.* σ_∞ [S cm^{-1}] and η_∞ [mPa s], the activation energy for ion conduction $E_{a\sigma}$ (eV), the dynamic viscosity activation energy $E_{a\eta}$ (eV) and the Boltzmann constant k_B (8.62x10^{-5} eV K^{-1}). The linearized VTF plots for the ionic conductivity and viscosity data are reported in Figure 4 (a-d), according to Equations 1 and 2. The equations' parameters are listed in Table 2 while the fitting results are reported in Figure S2. It is worth noting that the calculated activation energies are slightly lower than other reported for lithium [51] and sodium [52] based ionic liquids, but rather comparable to those of carbonate based electrolytes.[53]

Figure 4

Table 2

The physical-chemical properties of the electrolytes were also investigated in terms of density as reported in Figure 5 (a, b). In the investigated temperature range, both the NaFSI (Figure 5 (a)) and the NaTFSI (Figure 5 (b)) based electrolytes show a decrease of density (ρ) with increasing temperature in a linear relationship well described by Equation 3, in which A and B are fitting parameters.

$$\rho = A + BT \tag{3}$$

Figure 5

The fitted data are reported in Figure S3 and the corresponding results with the obtained A and B parameters are reported in Table S1. The lower densities are observed for the $Pyr_{14}TFSI$ based electrolytes, with a density value of about 1.35 g cm^{-3}. The mixed ionic liquid systems, *i.e.* F-14FT and T-14TF, present identical density value at 20 °C (1.39 g cm^{-3}). Overall, their densities differ by less than 6% and 3% within the NaFSI- and NaTFSI-based electrolytes, respectively. Based on the density values, the molar concentration is obtained and used to qualitatively estimate the ion dissociation, or ionicity[54] of the electrolytes by applying the Walden rule. This latter correlates the molar ionic conductivity and the viscosity through a temperature dependent constant (*K*) as reported in Equation 4.

$$\Lambda \eta = K \tag{4}$$

Λ represents the molar ionic conductivity obtained dividing the ionic conductivity (σ) by the molar concentration, which is the ratio of the density (ρ) and the formula weight. The Walden plots reporting the logarithm of the molar conductivity against the logarithm of the reciprocal of the viscosity are shown in Figure 5 (c-d). All the investigated blends lie just below the ideal line of the Walden plot, regardless of temperature.[44,52,54] This behaviour represents the ideal case in

which systems are characterized by low viscosity and high conductivity, suggesting for good ion mobility within the investigated temperature range. However, a deeper investigation offered by the linear fitting of the Walden plots (see Figure S4) suggest that the ionic conductivity of the electrolytes was slightly lower than those expected from their viscosities based on the Walden rule. Indeed, the slope of the Walden plots is slightly smaller than unit (see insets in Figure S4), varying from about 0.8 to 0.9 for both NaFSI and NaTFSI based blends. This may suggest a decrease of ionicity or higher degree of correlation between the cations and anions motion (*i.e.*, by association), which can be described by the fractional Walden rule in Equation 5:

$$\Lambda\eta^{\alpha} = K \tag{5}$$

where α, called the decoupling constant and ranging from zero to unity, corresponds to the slope of the Walden plot. The decrease of ionicity indicates an increasing deviation from the Walden rule. A comprehensive literature survey on the matter has been reported in previous papers.[54–56]

3.4. Electrochemical behaviour and structural stability of $Na_{0.6}Ni_{0.22}Al_{0.11}Mn_{0.66}O_2$ in IL - based electrolytes

The potential use of the investigated ionic liquids as electrolyte in sodium cells was evaluated by using a layered, P2-type $Na_{0.6}Ni_{0.22}Al_{0.11}Mn_{0.66}O_2$ cathode material. Previous results show that the electrode material exhibits an extraordinary reversible capacity when cycled within the 4.6 V-1.5 V voltage range in carbonate-based electrolytes.[40] However, as for most of the P2-type manganese based layered materials, the cycling performance is affected by the structural transitions occurring at the low- (2.0 V-1.5 V) and high-voltage (V > 4.0 V) regions.[57–59] In spite of the beneficial effect of aluminium on the structural stabilization at high voltage, the hexagonal

P2 to the orthorhombic P′2 phase transition, occurring at low voltage values and triggered by the Jahn–Teller effect of the active Mn^{3+} ions, still represents a limitation.[60]

In view of its high ionic conductivity, the T-13F electrolyte has been preliminary investigated in sodium cells by cycling the NAM cathode in the full voltage range, *i.e.* 4.6 V-1.5 V. As shown in Fig. S5, an initial discharge capacity of about 190 mAh g^{-1} is observed. However, after the 3rd cycle the capacity drops down to 180 mAh g^{-1} while side reactions occur at the end of the de-sodiation process. Indeed, above 3.5 V, the reaction of $Pyr_{13}FSI$ with the aluminium current collector and/or with the cell casing is observed.[61–63] Due to such a reactivity the $Pyr_{13}FSI$-based blends were not further analysed in sodium cells.

Figure 6

The investigation in the full potential range, *i.e.* 4.6 V-1.5 V, was also performed on cells using T-14F as the electrolyte (see Fig. 6 (a, b)). An extraordinary capacity of about 190 mAh g^{-1} is observed during the first cycles, however, a continuous capacity fading affected the cell. The potential profiles reported in Fig. 6 (a) clearly reveal the deleterious effect of the low voltage phase transition. Indeed, the length of the associated plateau is shortening upon cycling, while the upper plateau maintains its length to a certain extent. Moreover, Fig. 6 (b) evidences a very low Coulombic efficiency most likely related to parasitic reactions occurring at high voltage, involving electrolyte oxidation and leading to a poor reversibility of the overall charge/discharge process.

In order to clarify the origin of these processes, we further investigated the same system under different conditions, *i.e.*, increasing the temperature to 40 °C but lowering the high cut-off potential to 4.3 V. The results, reported in Fig. 6 (c) and (d), show improved cycling

performance in terms of Coulombic efficiency, i.e., reversibility of the process, due to the lower cut-off potential, in spite of the higher temperature expected to enhance side reactions, indicating the upper voltage cut-off as the reason for the low Coulombic efficiency. Interestingly, the increased temperature further enhances the cell delivered capacity, which after 10 cycles is comparable with that achieved using organic carbonate-based electrolytes.[40]

Nonetheless, the cell is still affected by a potential decay upon cycling in the low potential region. To further investigate the low voltage NAM behavior, additional galvanostatic tests were carried out in the 4.0 V-1.5 V voltage region (see Fig. 7). Additionally, the structural modifications occurring upon cycling were followed by *ex-situ* XRD measurements at different states of charge (see Fig. 8).

Figure 7

The cycling behaviour of the NaFSI- and NaTFSI-based electrolytes is shown, respectively, in Figure 7 (a) and (b). The $Pyr_{14}FSI$ containing cells (F-14F and T-14F blends) outperform others regardless the salt composition, with specific capacity approaching 140 mAh g^{-1} and capacity retention of about 100% for 200 cycles. The cells containing the $Pyr_{14}TFSI$ ionic liquid (Figure 7 (a, b)) exhibit poor electrochemical response. For the T-14T electrolyte a continuous capacity increase is observed over the first 30 cycles, suggesting a poor wettability of the electrode most likely related to the high viscosity of the electrolyte, and a poor cyclability of about 50 cycles (see Figure 3). The result may be explained considering the large size of the $[TFSI]^-$ anion, which is responsible of the lower mobility and higher viscosity of the T-14T electrolyte. Indeed, by substituting only 10% of $[TFSI]^-$ with the smaller $[FSI]^-$ (see F-14T electrolyte, Figure 7 (a)) the cycling performance is improved. The delivered capacity is constantly increasing over the first 75 cycles, stabilizing at 130 mAh g^{-1} up to 200 cycles.

Once more, the mixed ionic liquid-based electrolytes, *i.e.*, F-14FT and T-14TF (Figure 7 (a) and (b) respectively), show an intermediate behaviour. However, it is worth noting that the poor performance of $Pyr_{14}TFSI$ is much suppressed when mixed with $Pyr_{14}FSI$. As expected, the two electrolytes with mixed ionic liquids, *i.e.*, F-14FT and T-14TF, show practically identical performance with the minor differences being ascribable to the cell assembly.

Figure 7 (c-d) displays selected cell voltage profile upon cycling offering a clear image of the electrolytes' effect on the cell performance upon cycling. The F-14F-containing cell exhibited voltage curves perfectly overlapping upon the entire cycling test, highlighting its superior performance. The cell employing the T-14F electrolyte also exhibit excellent behaviour, however, displaying some polarization mostly occurring upon sodiation. Interestingly, this cell does not show any decrease in Coulombic efficiency toward the end of the test.

The electrochemical behaviour of the $Pyr_{14}TFSI$ ionic liquid containing cells (Figure 7 (d-g)) is rather poor being affected by voltage decay upon cycling and increased polarization most likely related to the low ionic conductivity ad high viscosity of the employed electrolytes. The cells containing mixed ionic liquids present an intermediate behaviour as indicated by the inferior polarization observed in the voltage profiles, slightly enhanced for the NaFSI based electrolyte. It is worth mentioning that the influence of the Na/electrolyte interface on the cycling behaviour of the NAM electrode (also known as electrode cross-talking) cannot be excluded. It has been reported that $[FSI]^-$ anion decomposition contributes to an improved stability of the passivation film formed at the anode side when compared to the $[TFSI]^-$ anion.[50] Thus, the improved cycling behaviour of the NAM electrode in the $[FSI]^-$-containing electrolytes might also be contributed from the more stable Na/electrolyte interface evolving.

In addition, it is worth noting that, considering only the most performing electrolytes, *i.e.*, F-14F and T-14F, the length of the low voltage plateau is not considerably changing upon cycling, thus suggesting an improved cyclability of the NAM due to the suppressed Mn dissolution.

Figure 8

The structural stability of the NAM electrode cycled in the most performing electrolytes, *i.e.*, T-14F and F-14F electrolyte, has been investigated through *ex-situ* XRD measurements. The analysis has been performed at different states of charge and cycle numbers. Herein, we report the study carried out by using F-14F electrolyte. The diffractograms of the pristine electrode, charged at 4.0 V, discharged at 2.0 V and fully discharged to 1.5 V during the 1st and 10th cycles are shown in Figure 8 (a).

The first two panels show the evolution of the *(002)* and *(004)* reflections, which are related to the *c* lattice parameter and thus to the distance between two successive MO_2 layers (interslab). By de-sodiating (charging) the electrode up to 4.0 V, the repulsion between the facing oxygen atoms on two consecutive MO_2 layers increases, thus increasing the interlayer distance on the *c* axis direction as demonstrated by the shift of the *(002)* and *(004)* reflections at lower 2θ values [59]. On the other hand, the *(10l)* reflections (see third panel), *i.e.* (*100*) and *(102)*, slightly shift to higher angles upon charge to 4.0 V. This indicates that the metal-to-metal distance within a metal oxide layer (related to the *a* lattice parameter) is decreasing while sodium is extracted, as a consequence of the transition metals oxidation upon de-sodiation.[64]

During the sodiation process down to 2.0 V, the (*002*) and (*004*) reflections shift to higher angles while new features appear at higher 2θ values (see new reflections indicated as $(002)_{P'2}$ and $(004)_{P'2}$ in Figure 8 (a)), indicating the appearance of a new P'2 phase co-existing with the

P2 phase. The P'2 phase is the result of an increasing concentration of Jahn-Teller active Mn^{3+} ions, a well-known process occurring in Mn-based layered oxides.[64,65] Indeed, the presence of Mn^{3+} ions leads to an orthorhombic distortion (space group: *Cmcm*) of the hexagonal P2-type structure (space group: $P6_3/mmc$).[66] In the distorted phase, here referred as P'2-type structure, the (*100*) and (*102*) peaks shift to lower angles during the discharge process. Upon further sodiation, when discharged up to 1.5 V, the electrode material structure completely converts to P'2 phase. Indeed the *(002)* and *(004)* peaks related to the P2 phase disappear while only the new $(002)_{P'2}$ and $(004)_{P'2}$ peaks are observed. In addition the *(100)* reflection disappears, while new features, here referred as $(022)_{P'2}$ and $(112)_{P'2}$, appear between 38 and 40 2θ value.

Interestingly, all the structural modification are reversible upon cycling. Indeed, the diffractogram of the de-sodiated electrode at the 10th cycle is perfectly overlapping with the de-sodiated electrode during the 1st charge. Additionally, the formation of the P'2 phase is also highly reversible as confirmed by the peak changes observed during the 10th cycle. The XRD study clearly demonstrates that the NAM material maintains its structural integrity undergoing fully reversible phase transitions upon cycling in the F-14F ionic liquid-based electrolyte.

Figure 8 (b) and (c) show a comparison of the voltage profile obtained by cycling the NAM electrode respectively in 1 M $NaPF_6$ in PC (propylene carbonate) and in F-14F (ionic liquid-based) electrolyte. It is clearly evidenced that the processes occurring upon (de-)sodiation are highly reversible in F-14F electrolyte (see Figure 8 (c)). Indeed, it is worth noticing that the low voltage plateau, which is shortening upon cycling when using 1 M $NaPF_6$ in PC (Figure 8 (b)), is much more stable by using F-14F electrolyte, evidencing even a slight increase in capacity after 50 cycles.

The observation justifies the improved cycling stability of the NAM electrode in the ionic liquid-based electrolyte, supersizing side-effects due to the presence of the Jahn-Teller Mn^{3+} ions. As a matter of fact, the phase transitions occur in both electrolyte solutions, indeed the formation of the P'2 phase is observed in the present work and in previously reported studies.[31,40,67] However, the Mn^{2+} formed as a consequence of the Jahn-Teller effect is not soluble in the ionic liquid-based electrolyte, thus further enhancing the structural stability and the reversibility of the phase transition, as demonstrated by the constant length of the low voltage plateau (see Figure 8 (c)). Overall, this study demonstrates that the cycling stability of NAM electrodes can be further improved by using room temperature F-14F (1:9 mol NaFSI in $Pyr_{14}FSI$) electrolyte. Furthermore, it demonstrates that tailoring ionic liquid-based electrolytes is an efficient strategy to mitigate the manganese dissolution of manganese-based layered oxides, which affects their electrochemical performance.

4. Conclusions

In this work, eight different pyrrolidinium-based ILs electrolytes, including single and binary anions mixtures, were fully characterized in terms of thermal, physical-chemical and electrochemical properties, aiming at their applications in room temperature SIBs. All the electrolytes presented high thermal stability up to 300 °C, with those including mixed anions, *i.e.*, F-14T, T-14F, F-14FT and T-14TF, showing very low tendency to crystallize, which represents a great advantage for room and sub-ambient temperature applications.

The wide ESW of all electrolytes allows their use with most of the electrode materials proposed for SIBs. All electrolytes exhibit ionic conductivities above 10^{-3} S cm^{-1} at room

temperature, with the $Pyr_{13}FSI$-based electrolytes exhibiting the highest values followed by $Pyr_{14}FSI$ and the mixed $Pyr_{14}FSI$:$Pyr_{14}TFSI$ systems.

The electrochemical behaviour at room temperature of such electrolytes in combination with the layered NAM cathode was also investigated. The electrolytes with 90 and 100 mol% $[TFSI]^-$ anion exhibited poor performance due to their high viscosity. On the other hand, those with 90 and 100 mol% $[FSI]^-$ anion enabled outstanding electrochemical performance of the cathode, delivering about 140 mAh g^{-1} for 200 cycles. This study suggests that the best performance in terms of conductivity, viscosity, thermal stability and electrochemical performance in sodium metal anode cells is achieved with the electrolyte containing only $[FSI]^-$, namely 1:9 mol NaFSI:$Pyr_{14}FSI$. The extraordinary cycling stability of the NAM electrodes in this electrolyte has been confirmed by ex-situ XRD study, indicating an improved capacity retention when compared to carbonate-based electrolyte. The study suggests a decreased solubility of Mn^{2+} formed as a consequence of the Jahn-Teller effect in the ionic liquid electrolyte, conferring enhanced cycling stability and reversibility of the phase transition occurring upon (de-)sodiation.

Associated content

Supporting Information:

Schematic of the sub-ambient annealing process performed on electrolytes during the DSC measurement. VTF-NLLSQ, linear fitting and obtained fitting parameters of electrolytes properties, *i.e.* conductivity, viscosity, density and ionicity. Cycling test of $Na/Na_{0.6}Ni_{0.22}Al_{0.11}Mn_{0.66}O_2$ cell in 1:9 mol NaTFSI in $Pyr_{13}FSI$.

Acknowledgements

The authors acknowledge Dr. Guk-Tae Kim, Dr. Guinevere Giffin and Dr. Huang Zhang for the valuable advices and the fruitful discussion. L.G.C. acknowledges the financial support from the Qatar National Research Fund (a member of Qatar Foundation), grant #NPRP9-263-2-122. The support of the Helmholtz Association is also acknowledged.

References

(1) Hightower, M.; Pierce, S. A. The Energy Challenge. *Nature* **2008**, *452* (7185), 285–286.

(2) Dell, R. M.; Rand, D. a J. Energy Storage - A Key Technology for Global Energy Sustainability. *J. Power Sources* **2001**, *100* (1–2), 2–17.

(3) Hall, P. J.; Bain, E. J. Energy-Storage Technologies and Electricity Generation. *Energy Policy* **2008**, *36* (12), 4352–4355.

(4) Goodenough, J. B.; Park, K. S. The Li-Ion Rechargeable Battery: A Perspective. *J. Am. Chem. Soc.* **2013**, *135* (4), 1167–1176.

(5) Scrosati, B. Recent Advances in Lithium Ion Battery Materials. *Electrochim. Acta* **2000**, *45* (15–16), 2461–2466.

(6) Wakihara, M.; Yamamoto, O.; Wakihara, M; Yamamoto, O. *Lithium Ion Batteries Fundamentals and Performance*; Wiley-VCH, 1998.

(7) Vaalma, C.; Buchholz, D.; Weil, M.; Passerini, S. A Cost and Resource Analysis of Sodium-Ion Batteries. *Nat. Rev. Mater.* **2018**, *3*, 18013.

(8) Masquelier, C.; Croguennec, L. Polyanionic (Phosphates, Silicates, Sulfates) Frameworks as Electrode Materials for Rechargeable Li (or Na) Batteries. *Chem. Rev.* **2013**, *113* (8), 6552–6591.

(9) Han, M. H.; Gonzalo, E.; Singh, G.; Rojo, T. A Comprehensive Review of Sodium Layered Oxides: Powerful Cathodes for Na-Ion Batteries. *Energy Environ. Sci.* **2015**, *8* (1), 81–102.

(10) Zhang, H.; Hasa, I.; Buchholz, D.; Qin, B.; Passerini, S. Effects of Nitrogen Doping on the Structure and Performance of Carbon Coated $Na_3V_2(PO_4)_3$ cathodes for Sodium-Ion Batteries. *Carbon N. Y.* **2017**, *124*, 334–341.

(11) Zhang, H.; Hasa, I.; Qin, B.; Diemant, T.; Buchholz, D.; Behm, R. J.; Passerini, S. Excellent Cycling Stability and Superior Rate Capability of $Na_3V_2(PO_4)_3$ Cathodes Enabled by Nitrogen-Doped Carbon Interpenetration for Sodium-Ion Batteries. *ChemElectroChem* **2017**, *4* (5) 1256-1263.

(12) Zhang, H.; Hasa, I.; Passerini, S. Beyond Insertion for Na-Ion Batteries: Nanostructured Alloying and Conversion Anode Materials. *Adv. Energy Mater.* **2018**, *8* (17) *1702582*.

(13) Muñoz-márquez, M. Á.; Saurel, D.; Gómez-cámer, J. L.; Casas-cabanas, M.; Castillo-martínez, E.; Rojo, T. Na-Ion Batteries for Large Scale Applications : A Review on Anode Materials and Solid Electrolyte Interphase Formation. *Adv. Energy Mater.* **2017**, *7* (20) *1700463*.

(14) Hasa, I.; Hassoun, J.; Passerini, S. Nanostructured Na -Ion and Li- Ion Anodes for Battery Application: A Comparative Overview. *Nano Res.* **2017**, *10* (12) *3942-3969.*

(15) Ponrouch, A.; Marchante, E.; Courty, M.; Tarascon, J.-M.; Palacín, M. R. In Search of an Optimized Electrolyte for Na-Ion Batteries. *Energy Environ. Sci.* **2012**, *5* (9), 8572-8583.

(16) Monti, D.; Jónsson, E.; Palacín, M. R.; Johansson, P. Ionic Liquid Based Electrolytes for Sodium-Ion Batteries: Na^+ Solvation and Ionic Conductivity. *J. Power Sources* **2014**, *245*, 630–636.

(17) Hasa, I.; Passerini, S.; Hassoun, J. Characteristics of an Ionic Liquid Electrolyte for Sodium-Ion Batteries. *J. Power Sources* **2016**, *303*, 203–207.

(18) Kalhoff, J.; Eshetu, G. G.; Bresser, D.; Passerini, S. Safer Electrolytes for Lithium-Ion Batteries: State of the Art and Perspectives. *ChemSusChem* **2015**, *8* (13), 2154–2175.

(19) Basile, A.; Bhatt, A. I.; O'Mullane, A. P. Stabilizing Lithium Metal Using Ionic Liquids for Long-Lived Batteries. *Nat. Commun.* **2016**, *7*, 1–11.

(20) Keller, M.; Schneider, M.; Sharova, V.; Kim, G.-T.; Schuhmacher, J.; Roters, A.; Passerini, S.; Appetecchi, G. B. Electrochemical Performance of a Solvent-Free Hybrid Ceramic-Polymer Electrolyte Based on $Li_7La_3Zr_2O_{12}$ in $P(EO)_{15}$LiTFSI. *J. Power Sources* **2017**, *353*, 287–297.

(21) MacFarlane, D. R.; Forsyth, M.; Howlett, P. C.; Kar, M.; Passerini, S.; Pringle, J. M.; Ohno, H.; Watanabe, M.; Yan, F.; Zheng, W.; Zhang, S.; Zhang, J. Ionic Liquids and Their Solid-State Analogues as Materials for Energy Generation and Storage. *Nat. Rev. Mater.* **2016**, *1*, 15005.

(22) Armand, M.; Endres, F.; MacFarlane, D. R.; Ohno, H.; Scrosati, B. Ionic-Liquid Materials for the Electrochemical Challenges of the Future. *Nat. Mater.* **2009**, *8* (8), 621–629.

(23) Toledo Hijo, A. A. C.; Maximo, G. J.; Costa, M. C.; Batista, E. A. C.; Meirelles, A. J. A. Applications of Ionic Liquids in the Food and Bioproducts Industries. *ACS Sustain. Chem. Eng.* **2016**, *4* (10), 5347–5369.

(24) Vekariya, R. L. A Review of Ionic Liquids: Applications towards Catalytic Organic Transformations. *J. Mol. Liq.* **2017**, *227*, 44-60.

(25) Acree, W.; Grubbs, L. Analytical Applications of Ionic Liquids. *Encycl. Anal. Chem.* **2012**, *12*, 329–355.

(26) Zhou, Y.; Qu, J. Ionic Liquids as Lubricant Additives: A Review. *ACS Appl. Mater. Interfaces* **2017**, *9* (4), 3209–3222.

(27) Rogers, R. D.; Seddon, K. R. Ionic Liquids-Solvents of the Future? *Science* **2003**, *302* (5646), 792–793.

(28) MacFarlane, D. R.; Meakin, P.; Sun, J.; Amini, N.; Forsyth, M. Pyrrolidinium Imides: A New Family of Molten Salts and Conductive Plastic Crystal Phases. *J. Phys. Chem. B*

1999, *103* (20), 4164–4170.

(29) Lewandowski, A.; Świderska-Mocek, A. Ionic Liquids as Electrolytes for Li-Ion Batteries-An Overview of Electrochemical Studies. *J. Power Sources* **2009**, *194* (2), 601–609.

(30) Wang, Y.; Zhong, W. H. Development of Electrolytes towards Achieving Safe and High-Performance Energy-Storage Devices: A Review. *ChemElectroChem* **2015**, *2* (1), 22–36.

(31) Chagas, L. G.; Buchholz, D.; Wu, L.; Vortmann, B.; Passerini, S. Unexpected Performance of Layered Sodium-Ion Cathode Material in Ionic Liquid-Based Electrolyte. *J. Power Sources* **2014**, *247*, 377–383.

(32) Li, J.; Jeong, S.; Kloepsch, R.; Winter, M.; Passerini, S. Improved Electrochemical Performance of $LiMO_2$ (M = Mn, Ni, Co)-Li_2MnO_3 Cathode Materials in Ionic Liquid-Based Electrolyte. *J. Power Sources* **2013**, *239*, 490–495.

(33) Hilder, M.; Gras, M.; Pope, C. R.; Kar, M.; MacFarlane, D. R.; Forsyth, M.; O'Dell, L. A. Effect of Mixed Anions on the Physicochemical Properties of a Sodium Containing Alkoxyammonium Ionic Liquid Electrolyte. *Phys. Chem. Chem. Phys.* **2017**, *19* (26), 17461–17468.

(34) Galiński, M.; Lewandowski, A.; Stepniak, I. Ionic Liquids as Electrolytes. *Electrochim. Acta* **2006**, *51* (26), 5567–5580.

(35) Eshetu, G. G.; Jeong, S.; Pandard, P.; Lecocq, A.; Marlair, G.; Passerini, S. Comprehensive Insights into the Thermal Stability, Biodegradability, and Combustion Chemistry of Pyrrolidinium-Based Ionic Liquids. *ChemSusChem* **2017**, *10* (15), 3146–3159.

(36) Kerner, M.; Plylahan, N.; Scheers, J.; Johansson, P. Ionic Liquid Based Lithium Battery

Electrolytes: Fundamental Benefits of Utilising Both TFSI and FSI Anions? *Phys. Chem. Chem. Phys.* **2015**, *17* (29), 19569–19581.

(37) Serra Moreno, J.; Maresca, G.; Panero, S.; Scrosati, B.; Appetecchi, G. B. Sodium-Conducting Ionic Liquid-Based Electrolytes. *Electrochem. commun.* **2014**, *43*, 1–4.

(38) Kunze, M.; Jeong, S.; Paillard, E.; Winter, M.; Passerini, S. Melting Behavior of Pyrrolidinium-Based Ionic Liquids and Their Binary Mixtures. *J. Phys. Chem. C* **2010**, *114* (28), 12364–12369.

(39) E. Visser, A.; J. Bridges, N.; D.Rogers, R. *Ionic Liquids: Science and Applications*; American Chemical Society, Washington DC: Washington, DC, 2012.

(40) Hasa, I.; Passerini, S.; Hassoun, J. Toward High Energy Density Cathode Materials for Sodium-Ion Batteries: Investigating the Beneficial Effect of Aluminum Doping on the P2-Type Structure. *J. Mater. Chem. A* **2017**, *5* (9), 4467–4477.

(41) Montanino, M.; Alessandrini, F.; Passerini, S.; Appetecchi, G. B. Water-Based Synthesis of Hydrophobic Ionic Liquids for High-Energy Electrochemical Devices. *Electrochim. Acta* **2013**, *96*, 124–133.

(42) Moosbauer, D.; Zugmann, S.; Amereller, M.; Gores, H. J. Effect of Ionic Liquids as Additives on Lithium Electrolytes: Conductivity, Electrochemical Stability, and Aluminum Corrosion. *J. Chem. Eng. Data* **2010**, *55* (5), 1794–1798.

(43) Monti, D.; Ponrouch, A.; Palacín, M. R.; Johansson, P. Towards Safer Sodium-Ion Batteries via Organic Solvent/Ionic Liquid Based Hybrid Electrolytes. *J. Power Sources* **2016**, *324*, 712–721.

(44) Moreno, M.; Simonetti, E.; Appetecchi, G. B.; Carewska, M.; Montanino, M.; Kim, G.-T.; Loeffler, N.; Passerini, S. Ionic Liquid Electrolytes for Safer Lithium Batteries. *J.*

Electrochem. Soc. **2017**, *164* (1), A6026–A6031.

(45) Garcia, B.; Armand, M. Aluminium Corrosion in Room Temperature Molten Salt. *J. Power Sources* **2004**, *132* (1–2), 206–208.

(46) Peng, C.; Yang, L.; Zhang, Z.; Tachibana, K.; Yang, Y.; Zhao, S. Investigation of the Anodic Behavior of Al Current Collector in Room Temperature Ionic Liquid Electrolytes. *Electrochim. Acta* **2008**, *53* (14), 4764–4772.

(47) Otaegui, L.; Goikolea, E.; Aguesse, F.; Armand, M.; Rojo, T.; Singh, G. Effect of the Electrolytic Solvent and Temperature on Aluminium Current Collector Stability: A Case of Sodium-Ion Battery Cathode. *J. Power Sources* **2015**, *297*, 168–173.

(48) Komaba, S.; Murata, W.; Ishikawa, T.; Yabuuchi, N.; Ozeki, T.; Nakayama, T.; Ogata, A.; Gotoh, K.; Fujiwara, K. Electrochemical Na Insertion and Solid Electrolyte Interphase for Hard-Carbon Electrodes and Application to Na-Ion Batteries. *Adv. Funct. Mater.* **2011**, *21* (20), 3859–3867.

(49) Alcántara, R.; Jiménez-Mateos, J. M.; Lavela, P.; Tirado, J. L. Carbon Black: A Promising Electrode Material for Sodium-Ion Batteries. *Electrochem. commun.* **2001**, *3* (11), 639–642.

(50) Elia, G. A.; Ulissi, U.; Jeong, S.; Passerini, S.; Hassoun, J. Exceptional Long-Life Performance of Lithium-Ion Batteries Using Ionic Liquid-Based Electrolytes. *Energy Environ. Sci.* **2016**, *9* (10), 3210–3220.

(51) Giffin, G.; Moretti, A.; Jeong, S.; Pilar, K.; Brinkkoetter, M.; Greenbaum, S.; Schoenhoff, M.; Passerini, S. Connection between Lithium Coordination and Lithium Diffusion in $Pyr_{12O1}FTFSI$ Ionic Liquid Electrolytes. *ChemSusChem* **2017**, *11* (12), 1981–1989.

(52) Matsumoto, K.; Okamoto, Y.; Nohira, T.; Hagiwara, R. Thermal and Transport Properties

of Na[$N(SO_2F)_2$]–[*N*-Methyl-*N*-Propylpyrrolidinium][$N(SO_2F)_2$] Ionic Liquids for Na Secondary Batteries. *J. Phys. Chem. C* **2015**, *119* (14), 7648–7655.

(53) Perera, K.; Dissanayake, M. Conductivity Variation of the Liquid Electrolyte, EC:PC:$LiCF_3SO_3$ with Salt Concentration. *Sri Lankan J. Phys.* **2006**, *7*, 1–5.

(54) MacFarlane, D. R.; Forsyth, M.; Izgorodina, E. I.; Abbott, A. P.; Annat, G.; Fraser, K. On the Concept of Ionicity in Ionic Liquids. *Phys. Chem. Chem. Phys.* **2009**, *11* (25), 4962–4967.

(55) Schreiner, C.; Zugmann, S.; Hartl, R.; Gores, H. J. Temperature Dependence of Viscosity and Specific Conductivity of Fluoroborate-Based Ionic Liquids in Light of the Fractional Walden Rule and Angell's Fragility Concept. *J. Chem. Eng. Data* **2010**, *55* (10), 4372–4377.

(56) Schreiner, C.; Zugmann, S.; Hartl, R.; Gores, H. J. Fractional Walden Rule for Ionic Liquids: Examples from Recent Measurements and a Critique of the so-Called Ideal KCl Line for the Walden Plot. *J. Chem. Eng. Data* **2010**, *55* (5), 1784–1788.

(57) Yabuuchi, N.; Kajiyama, M.; Iwatate, J.; Nishikawa, H.; Hitomi, S.; Okuyama, R.; Usui, R.; Yamada, Y.; Komaba, S. P2-Type $Na_x[Fe_{1/2}Mn_{1/2}]O_2$ Made from Earth-Abundant Elements for Rechargeable Na Batteries. *Nat. Mater.* **2012**, *11* (6), 512–517.

(58) Lee, D. H.; Xu, J.; Meng, Y. S. An Advanced Cathode for Na-Ion Batteries with High Rate and Excellent Structural Stability. *Phys. Chem. Chem. Phys.* **2013**, *15* (9), 3304–3312.

(59) Zhonghua Lu; Dahn, J. R. In Situ X-Ray Diffraction Study of P2-$Na_{2/3}Ni_{1/3}Mn_{2/3}O_2$. *J. Electrochem. Soc.* **2001**, *148* (11), A1225–A1229.

(60) Mortemard De Boisse, B.; Carlier, D.; Guignard, M.; Bourgeois, L.; Delmas, C. P2-

$Na_xMn_{1/2}Fe_{1/2}O_2$ Phase Used as Positive Electrode in Na Batteries: Structural Changes Induced by the Electrochemical (De)Intercalation Process. *Inorg. Chem.* **2014**, *53* (20), 11197–11205.

(61) Evans, T.; Olson, J.; Bhat, V.; Lee, S. H. Corrosion of Stainless Steel Battery Components by Bis(Fluorosulfonyl)Imide Based Ionic Liquid Electrolytes. *J. Power Sources* **2014**, *269*, 616–620.

(62) Evans, T.; Olson, J.; Bhat, V.; Lee, S. H. Effect of Organic Solvent Addition to $PYR_{13}FSI$ + LiFSI Electrolytes on Aluminum Oxidation and Rate Performance of $Li(Ni_{1/3}Mn_{1/3}Co_{1/3})O_2$ cathodes. *J. Power Sources* **2014**, *265*, 132–139.

(63) Cho, E.; Mun, J.; Chae, O. B.; Kwon, O. M.; Kim, H. T.; Ryu, J. H.; Kim, Y. G.; Oh, S. M. Corrosion/Passivation of Aluminum Current Collector in Bis(Fluorosulfonyl) Imide-Based Ionic Liquid for Lithium-Ion Batteries. *Electrochem. commun.* **2012**, *22* (1), 1–3.

(64) Talaie, E.; Duffort, V.; Smith, H.; Fultz, B.; Nazar, L. Structure of the High Voltage Phase of Layered P2-$Na_{2/3-x}[Mn_{1/2}Fe_{1/2}]O_2$ and the Positive Effect of Ni Substitution on Its Stability. *Energy Environ. Sci.* **2015**, *8*, 2512–2523.

(65) Dose, W. M.; Sharma, N.; Pramudita, J. C.; Kimpton, J. A.; Gonzalo, E.; Han, M. H.; Rojo, T. Cystallographic Evolution of P2 $Na_{2/3}Fe_{0.4}Mn_{0.6}O_2$ Electrodes during Electrochemical Cycling. *Chem. Mater.* **2016**, *28* (17), 6342–6354.

(66) Talaie, E.; Kim, S. Y.; Chen, N.; Nazar, L. F. Structural Evolution and Redox Processes Involved in the Electrochemical Cycling of P2-$Na_{0.67}[Mn_{0.66}Fe_{0.20}Cu_{0.14}]O_2$. *Chem. Mater.* **2017**, *29* (16), 6684–6697.

(67) Wang, H.; Gao, R.; Li, Z.; Sun, L.; Hu, Z.; Liu, X. Different Effects of Al Substitution for Mn or Fe on the Structure and Electrochemical Properties of $Na_{0.67}Mn_{0.5}Fe_{0.5}O_2$ as a

Sodium Ion Battery Cathode Material. *Inorg. Chem.* **2018**, *57* (9), 5249–5257.

Electrolyte code	*Salt*	*Ionic Liquid (IL)*		***NaX:IL$_1$:IL$_2$ molar ratio***	*[FSI]$^-$/[TFSI]$^-$ ratio*
F-13F	NaFSI	$PYR_{13}FSI$		1:9	100:0
F-14F		$PYR_{14}FSI$		1:9	100:0
F-14T		$PYR_{14}TFSI$		1:9	10:90
F-14FT		$PYR_{14}FSI$	$PYR_{14}TFSI$	1:4:5	50:50
T-13F	NaTFSI	$PYR_{13}FSI$		1:9	90:10
T-14F		$PYR_{14}FSI$		1:9	90:10
T-14T		$PYR_{14}TFSI$		1:9	0:100
T-14TF		$PYR_{14}TFSI$	$PYR_{14}FSI$	1:4:5	50:50

Table 1. Nomenclature and composition of the investigated electrolytes.

Ionic Conductivity			
Electrolyte	σ_∞ *[S cm^{-1}]*	E_a *[eV]*	T_0 *[K]*
F-13F	0.53 ± 0.03	$5.3\cdot10^{-2} \pm 0.1\cdot10^{-2}$	159 ± 2
F-14F	0.53 ± 0.03	$5.6\cdot10^{-2} \pm 0.1\cdot10^{-2}$	162 ± 2
F-14T	0.51 ± 0.04	$6.0\cdot10^{-2} \pm 0.2\cdot10^{-2}$	177 ± 2
F-14FT	0.57 ± 0.04	$5.8\cdot10^{-2} \pm 0.1\cdot10^{-2}$	171 ± 2
T-13F	0.50 ± 0.04	$5.3\cdot10^{-2} \pm 0.2\cdot10^{-2}$	164 ± 2
T14-F	0.52 ± 0.03	$5.6\cdot10^{-2} \pm 0.1\cdot10^{-2}$	172 ± 2
T-14T	0.38 ± 0.03	$5.9\cdot10^{-2} \pm 0.2\cdot10^{-2}$	180 ± 2
T-14TF	0.52 ± 0.03	$5.6\cdot10^{-2} \pm 0.1\cdot10^{-2}$	172 ± 2
Viscosity			
Electrolyte	η_∞ *[mPa s]*	E_a *[eV]*	T_0 *[K]*
F-13F	0.256 ± 0.009	$6.79\cdot10^{-2} \pm 0.06\cdot10^{-2}$	152.7 ± 0.5
F-14F	0.191 ± 0.005	$7.72\cdot10^{-2} \pm 0.04\cdot10^{-2}$	147.8 ± 0.4
F-14T	0.008 ± 0.005	$8.71\cdot10^{-2} \pm 0.09\cdot10^{-2}$	160.5± 0.5
F-14FT	0.138 ± 0.007	$7.92\cdot10^{-2} \pm 0.09\cdot10^{-2}$	157.2 ± 0.6
T-13F	0.302 ± 0.007	$6.49\cdot10^{-2} \pm 0.04\cdot10^{-2}$	152.7 ± 0.4
T14-F	0.167 ± 0.005	$7.83\cdot10^{-2} \pm 0.06\cdot10^{-2}$	149.2 ± 0.4
T-14T	0.075 ± 0.004	$8.72\cdot10^{-2} \pm 0.08\cdot10^{-2}$	165.4± 0.4
T-14TF	0.155 ± 0.006	$7.45\cdot10^{-2} \pm 0.07\cdot10^{-2}$	160.9 ± 0.5

Table 2. Value of the ionic conductivity at infinite temperature (σ_∞), maximum dynamic viscosity (η_∞), activation energy (E_a) and zero configurational entropy (T_0) obtained by the VTF fit of the conductivity and viscosity plots.

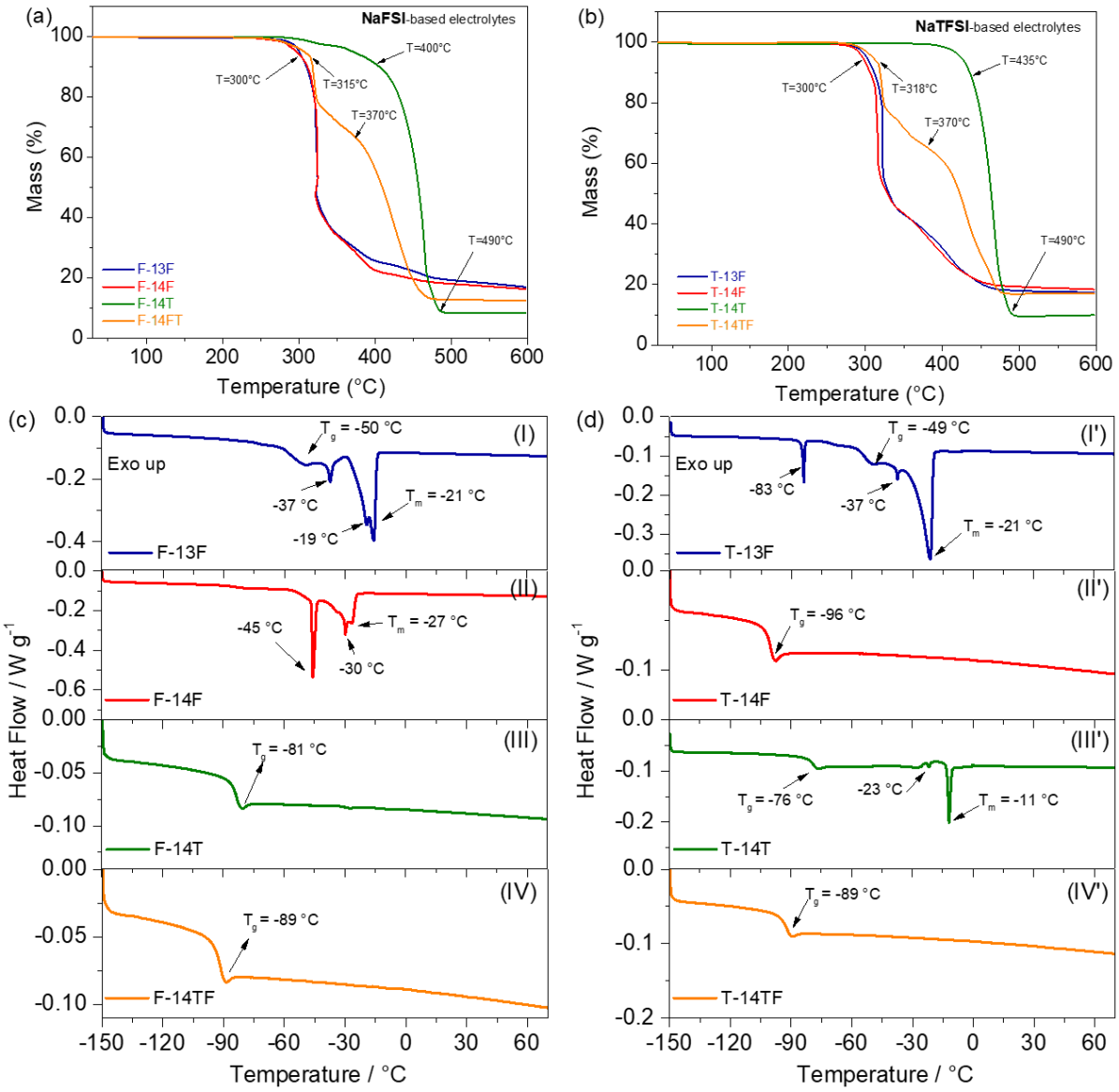

Figure 1. TG analysis of the (a) NaFSI and (b) NaTFSI based electrolytes obtained under N_2 flux heating from 30 °C to 600 °C at 10 °C min^{-1} scan rate. DSC heating traces of (c) NaFSI and (d) NaTFSI based electrolytes obtained during heating from -150 °C to 80 °C, after sub-ambient annealing.

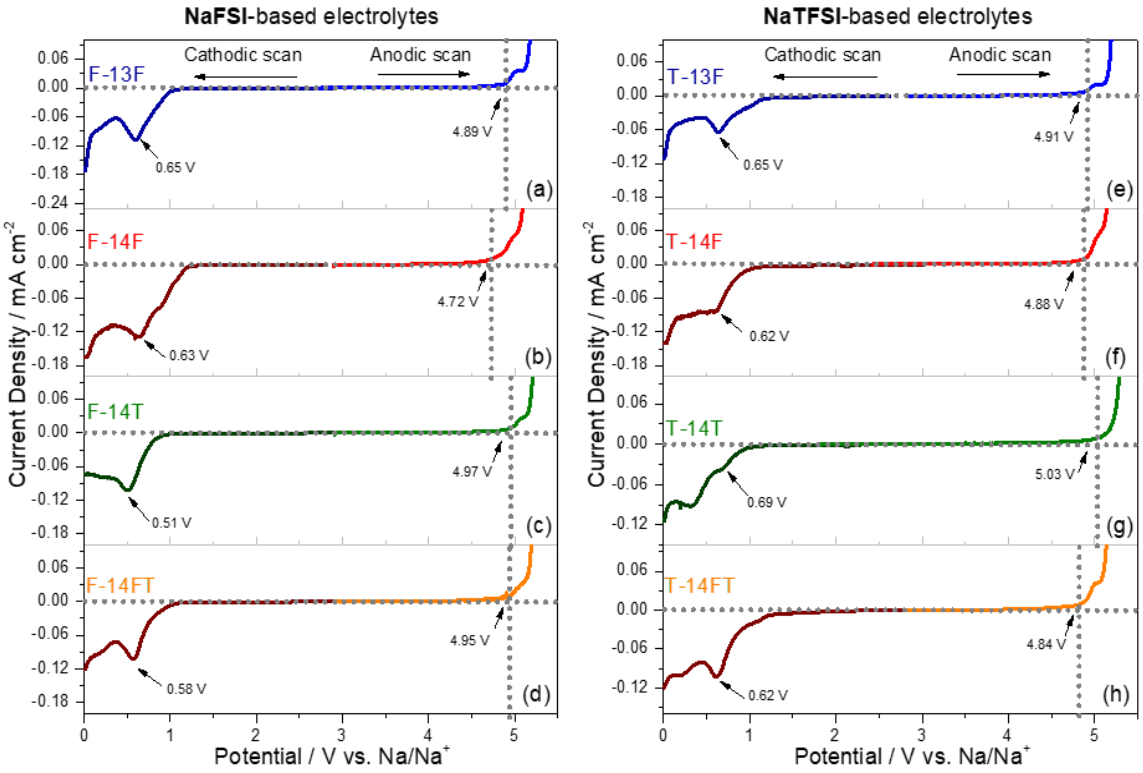

Figure 2. Electrochemical stability window (ESW) of the (a-d) NaFSI and (e-h) NaTFSI based electrolytes determined using carbon black working electrode. Tests run at 0.1 mV s^{-1} at room temperature in three-electrode cells, employing Na metal as counter and reference electrodes.

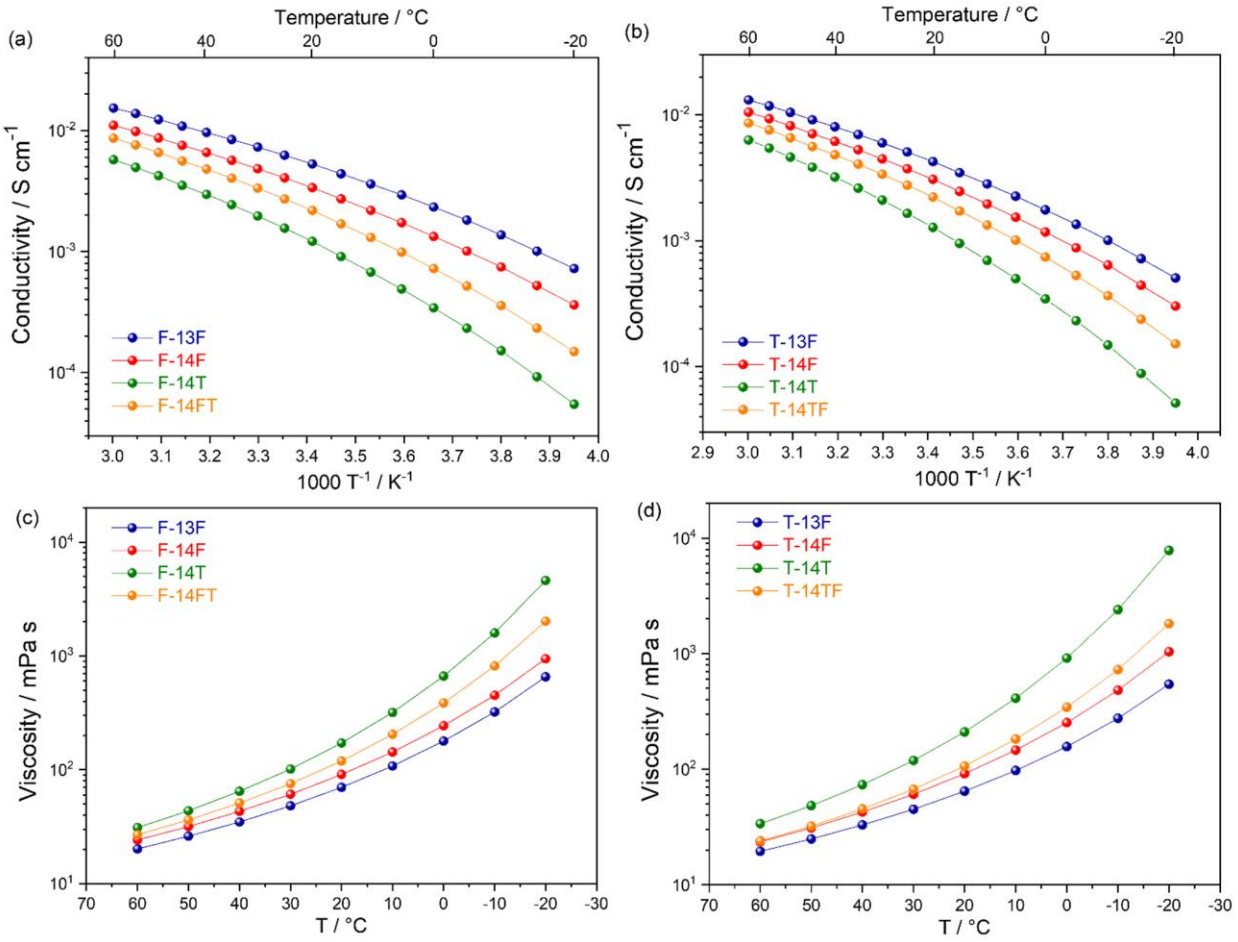

Figure 3. Arrhenius plots of conductivity *vs.* temperature dependence of (a) NaFSI and (b) NaTFSI based electrolytes. Viscosity trend within the same temperature range for (c) NaFSI and (d) NaTFSI blends.

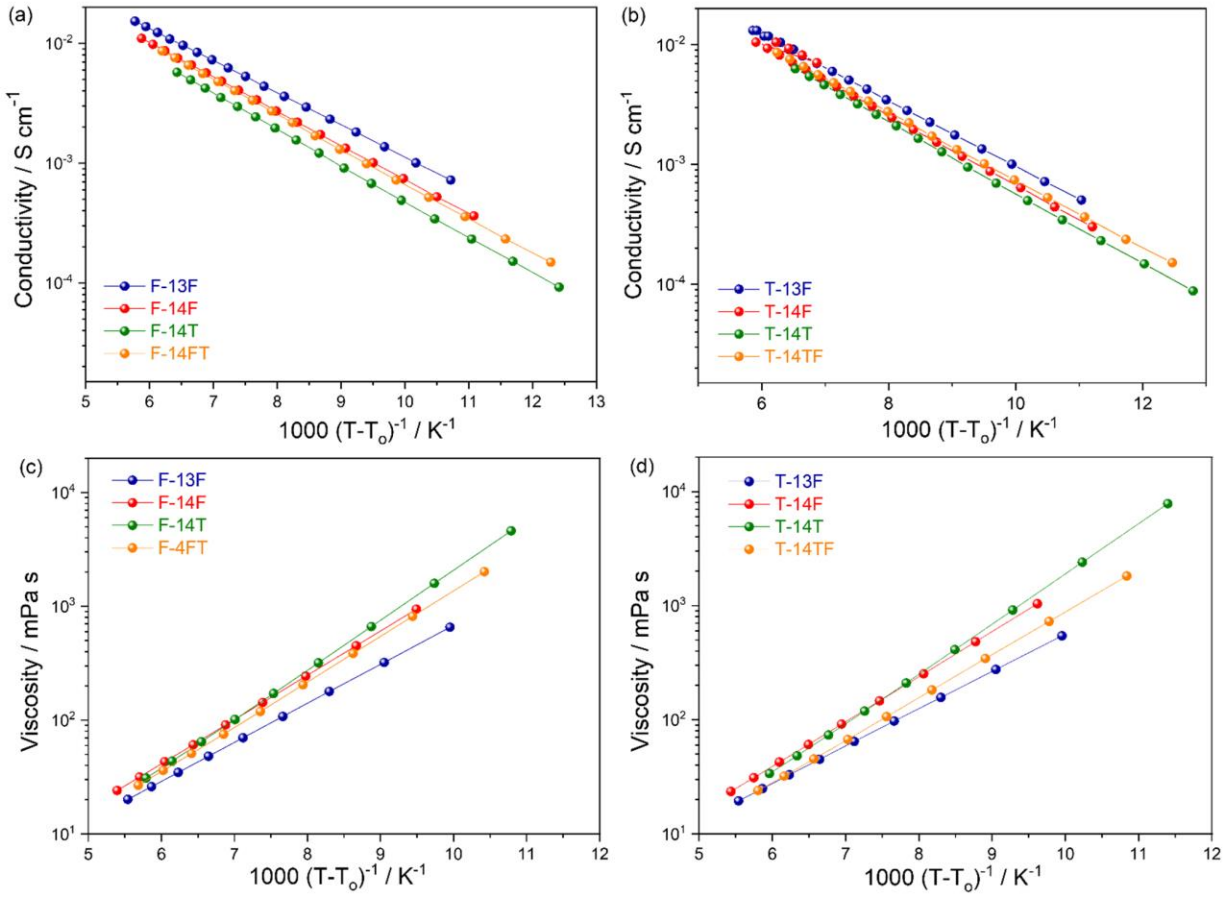

Figure 4. (a-b) Conductivity and (c-d) viscosity Vogel–Tammann–Fulcher (VTF) linearized plots reported *versus* 1000/(T-T_0) for (a, c) NaFSI and (b, d) NaTFSI based electrolytes.

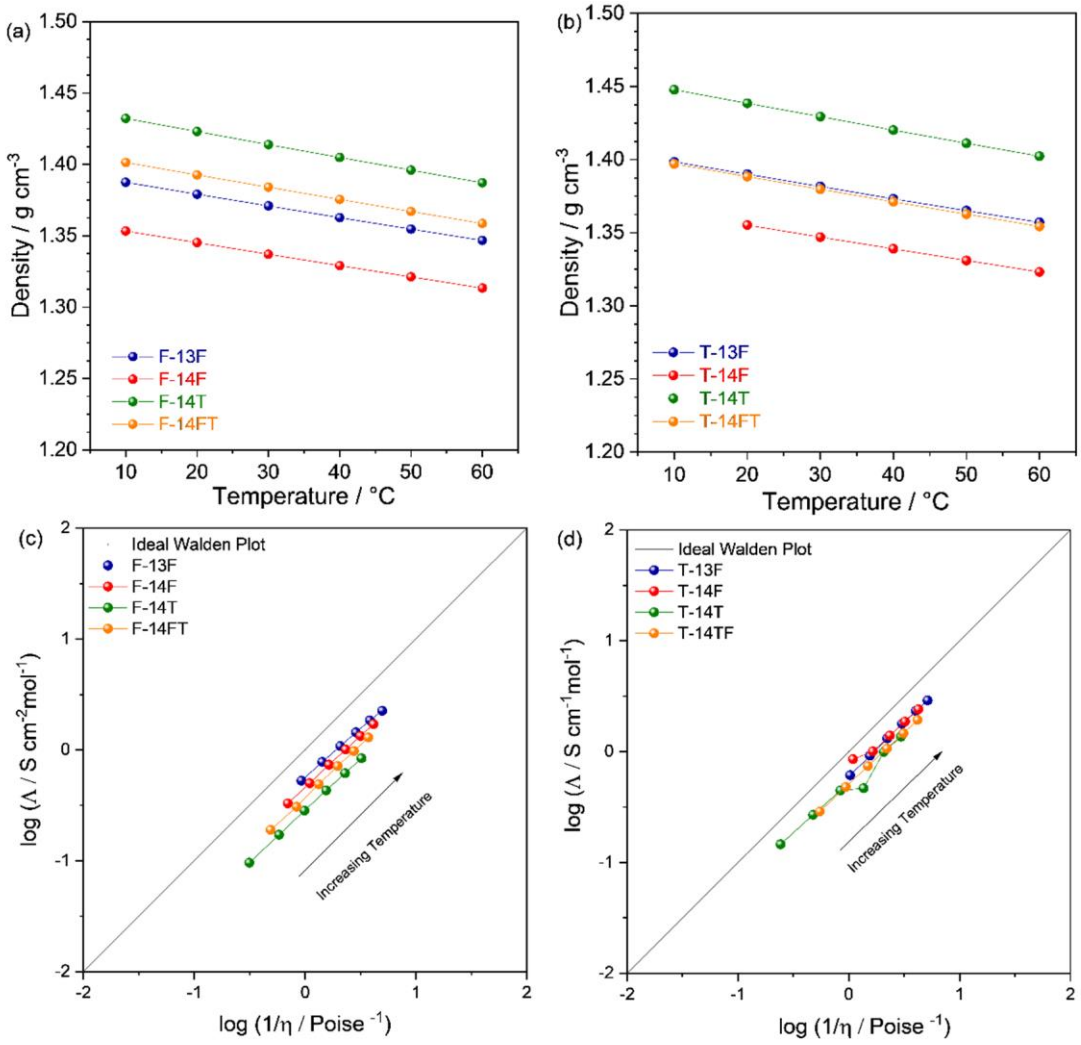

Figure 5. Density *vs.* temperature dependence of (a) NaFSI and (b) NaTFSI based electrolytes. Walden plots for the (c) NaFSI and (d) NaTFSI based blends. The straight line represents the ideal Walden behavior.

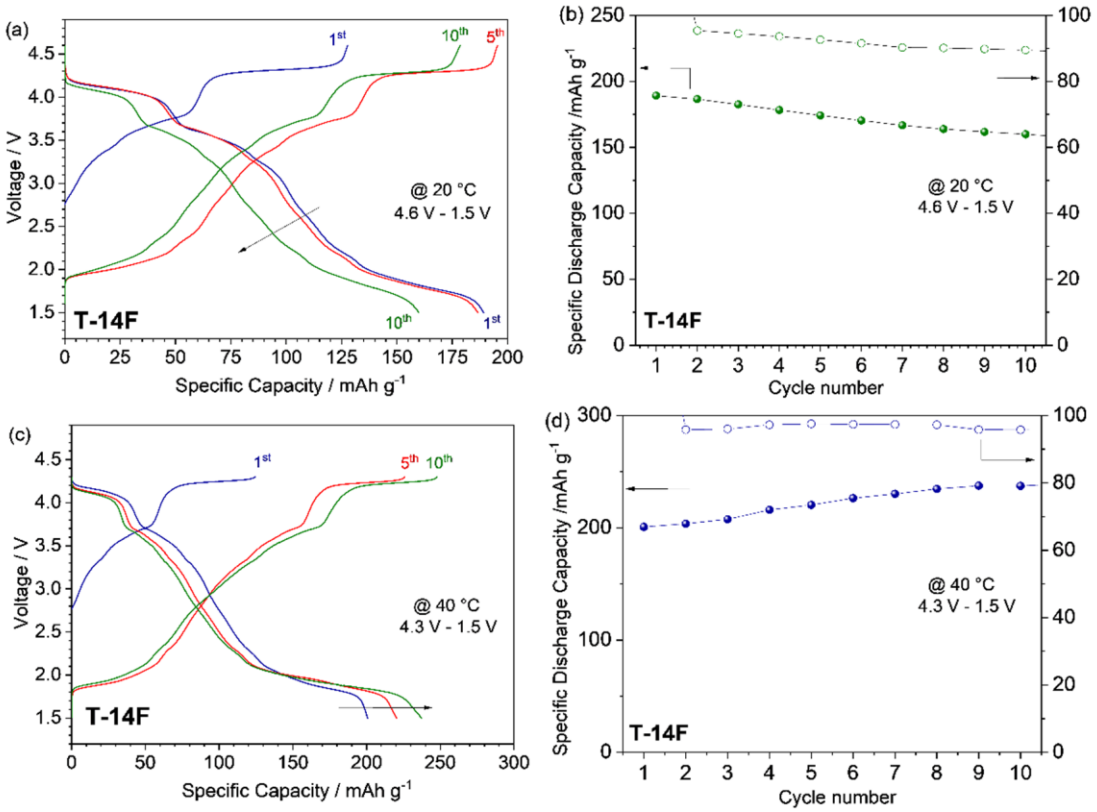

Figure 6. Selected galvanostatic charge/discharge profiles and cycling behavior of $Na//Na_{0.6}Ni_{0.22}Al_{0.11}Mn_{0.66}O_2$ cells performed at (a, b) 20 °C within the 4.6 V - 1.5 V voltage range and at (c, d) 40 °C within the 4.3 V - 1.5 V voltage range. Tests run at 30 mA g^{-1} by using 1:9 mol NaTFSI in $PYR_{14}FSI$ electrolyte in three-electrode cell, with Na metal as counter and reference electrodes.

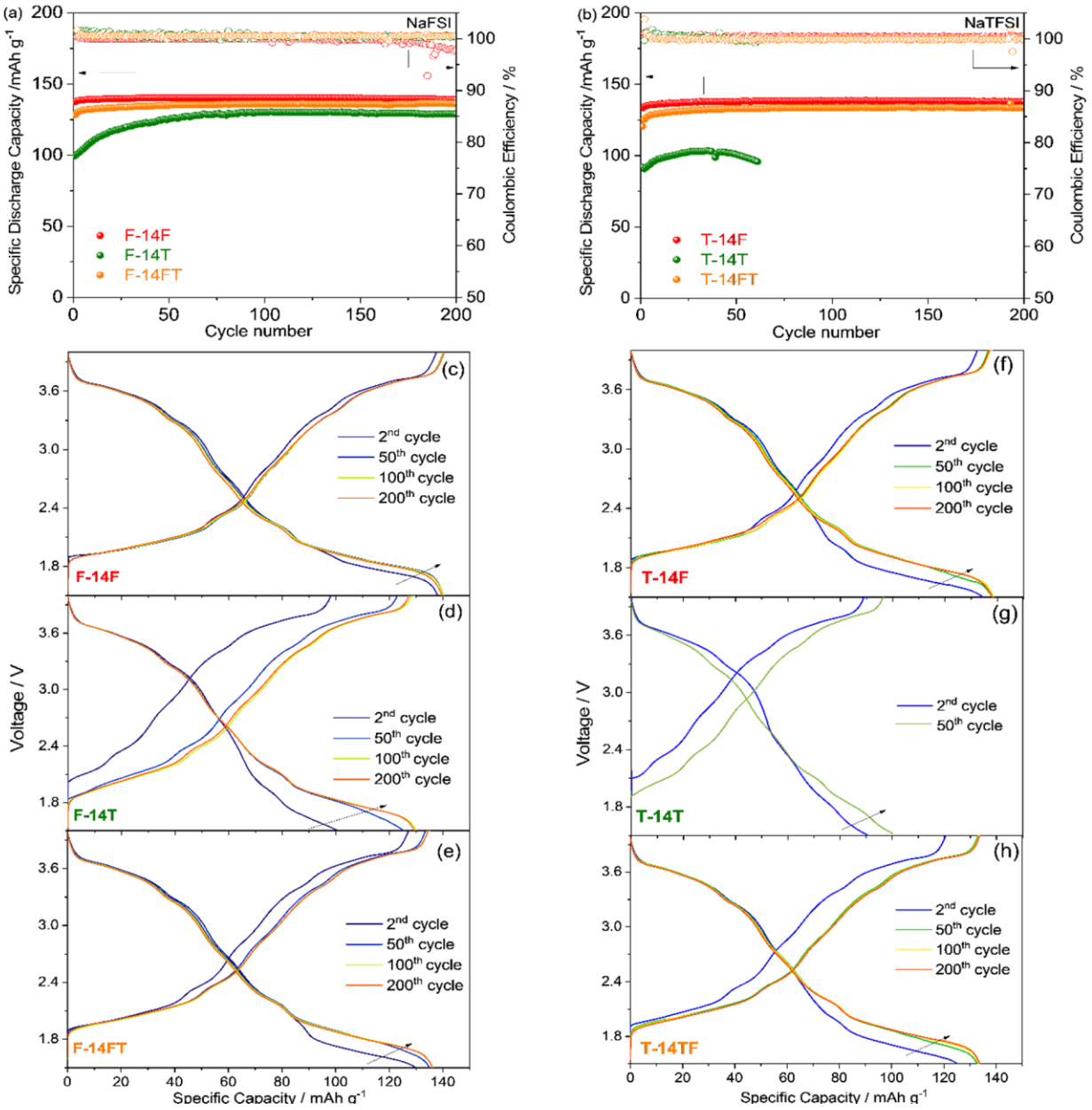

Figure 7. Cycling behavior and selected galvanostatic charge/discharge profiles of Na//$Na_{0.6}Ni_{0.22}Al_{0.11}Mn_{0.66}O_2$ cells performed at 30 mA g^{-1} within the 4.0 V - 1.5 V voltage range in presence of different electrolytes containing (a, c-e) NaFSI or (b, f-h) NaTFSI salts and different ionic liquids. Arrows indicate the cycling evolution.

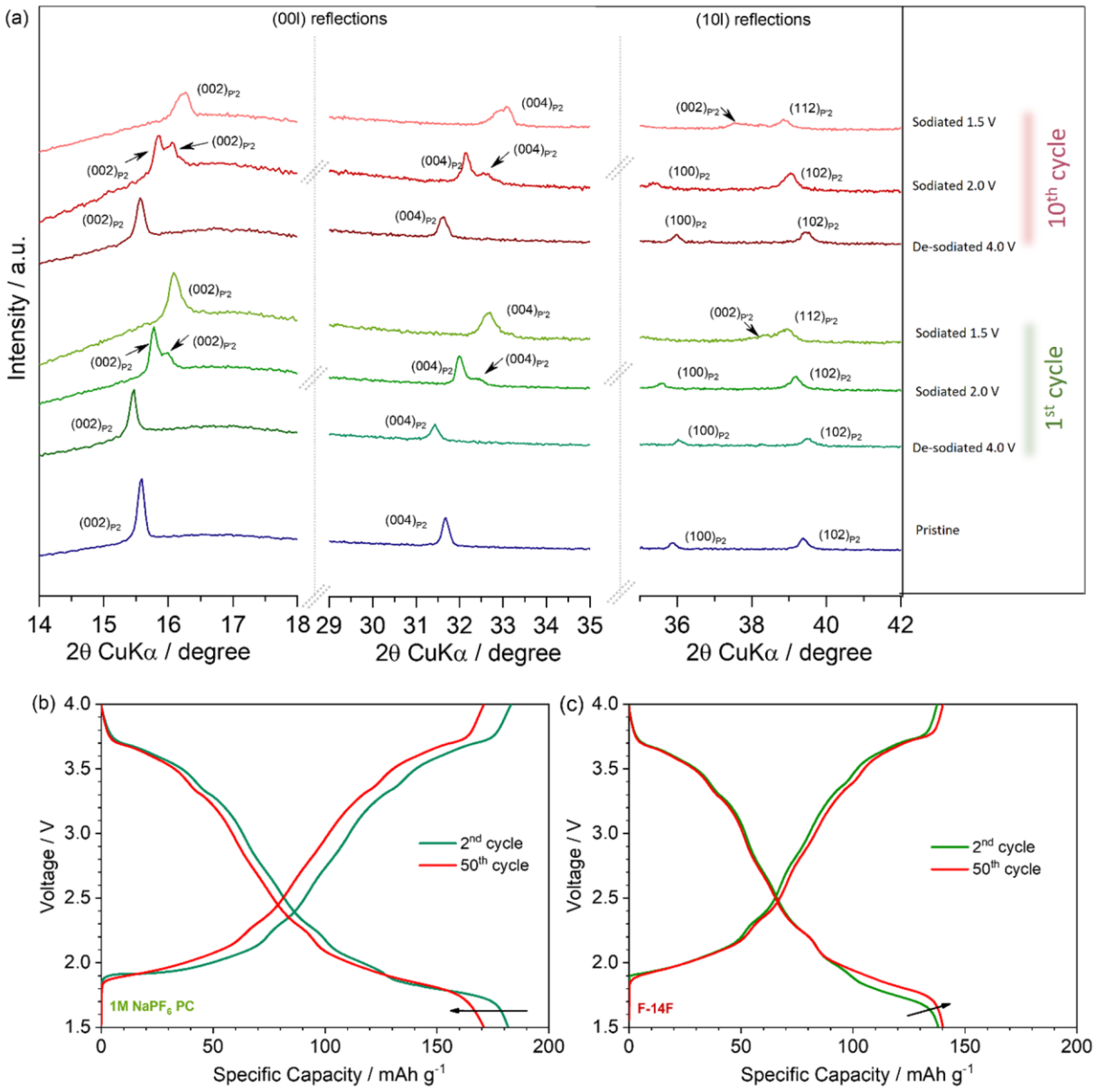

Figure 8. (a) *Ex-situ* XRD study on NAM electrodes cycled in F-14F electrolyte. The diffractograms report the changes for the *(00l)* and *(10l)* reflections during the 1st and 10th cycle at 4.0 V upon de-sodiation, 2.0 V and 1.5 V upon sodiation. Selected galvanostatic charge/discharge profiles of $Na/Na_{0.6}Ni_{0.22}Al_{0.11}Mn_{0.66}O_2$ cells performed at 30 mA g^{-1} within 4.0 V - 1.5 V voltage range by using 1 M $NaPF_6$ in PC (propylene carbonate) (b) and F-14F (c) as electrolyte solution.

For Table of Contents Only:

Graphical abstracts

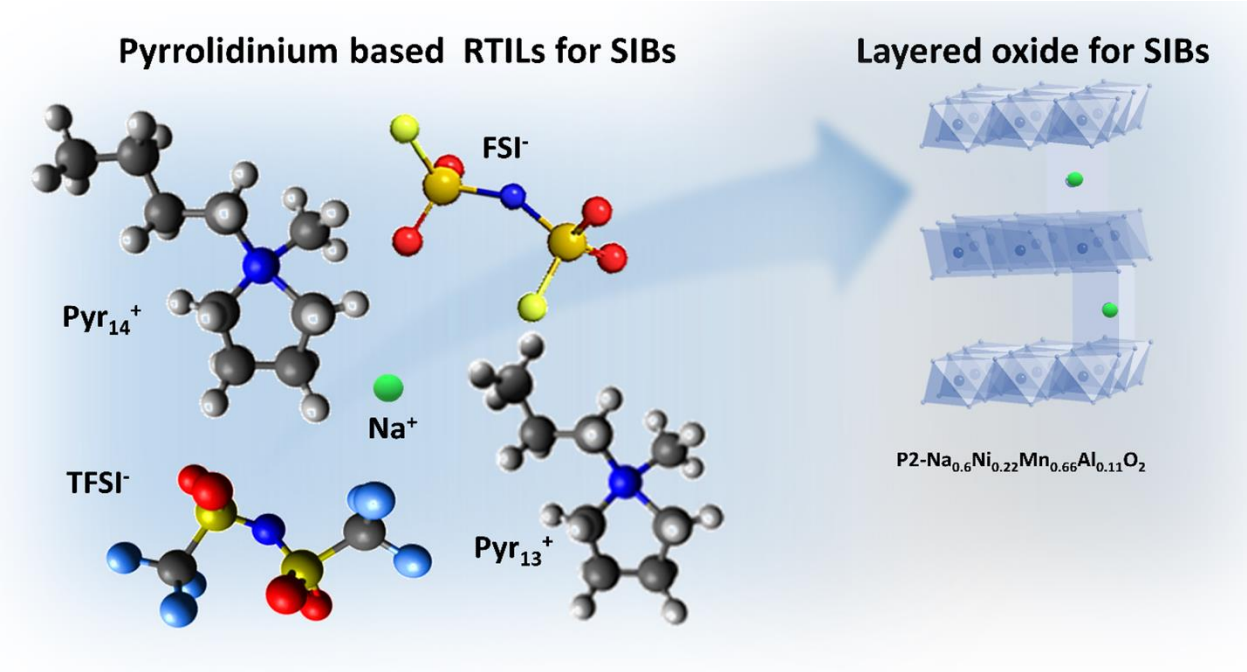

Pyrrolidinium based ionic liquids enhance the cycling stability of room temperature sodium batteries using a layered P2-$Na_{0.6}Ni_{0.22}Al_{0.11}Mn_{0.66}O_2$ cathode.